

Three-Dimensional Molecular Orientation Imaging of a Semicrystalline Polymer Film under Shear Deformation

Shuyu Xu, Chad R. Snyder, Jeremy Rowlette, and Young Jong Lee*



Cite This: <https://doi.org/10.1021/acs.macromol.1c02036>



Read Online

ACCESS |



Metrics & More

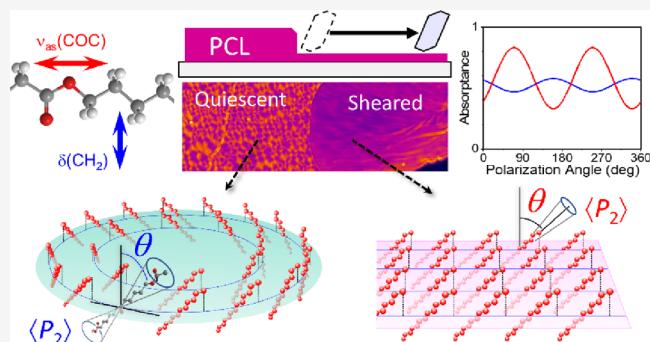


Article Recommendations



Supporting Information

ABSTRACT: The 3D molecular orientations of polymer chains are imaged and compared for a quiescent spherulite region and a shear-deformed region of a semicrystalline poly(ϵ -caprolactone) film. To acquire the images of 3D orientation, we used a newly developed hyperspectral imaging method based on the orthogonal-pair polarization IR (OPPIR) analysis. Polymer chains in spherulites are azimuthally aligned perpendicular to the crystal growth direction and axially tilted from the film normal direction. By contrast, polymer chains in a sheared region are azimuthally aligned along the shear direction but axially tilted from the shear direction. The unexpected out-of-plane tilted orientation indicates that orientational relaxation followed shear deformation and occurred predominantly in the out-of-plane direction. Furthermore, incorporating peak deconvolution into the OPPIR analysis shows that the crystalline and amorphous chains are oriented aligned at different angles, possibly due to different orientational relaxation between the two chain configurations.



INTRODUCTION

Mechanical shape deformation of polymers can accompany significant changes in molecular orientation, and the anisotropic alignment of polymer chains often occurs in three dimensions (3D) and heterogeneously at different length scales.^{1–3} Accurate measurements of molecular orientation with a sufficiently high spatial resolution will facilitate a better understanding of the structure–property relationship of polymers and thus will advance the manufacturing productivity of high-performance materials. However, conventional tomographic methods for 3D orientation measurement,⁴ e.g., X-ray scattering,^{5,6} transmission electron microscopy (TEM) diffraction,^{7,8} and sample-tilting infrared (IR) dichroism,^{9–11} are not suitable for large-area imaging because of sample tilting. By contrast, other imaging methods with high resolving power have been developed to map the molecular orientation by detecting polarization-controlled optical signals, such as fluorescence,^{12,13} second harmonic generation,¹⁴ Raman scattering,^{15–18} and IR absorption.^{19–23} However, the single-mode 2D-projected orientation approaches cannot determine the out-of-plane angle of molecular orientation and thus cannot provide accurate 3D orientational information; therefore, they can be used as quantitative measurement tools only when the molecular symmetry axis is confirmed to lie in the plane normal to the light propagation direction, e.g., fibers²⁴ and highly stretched films.²⁵

IR microscopy can be used for label-free chemical imaging by detecting fingerprint modes of intrinsic molecules in various materials, such as biological tissues,¹⁹ biopolymers,²⁰ and

polymer films.^{21–23} Additionally, the quantitative nature of the IR absorbance allows for mapping of absolute concentration and polarization anisotropy that can be interlaboratory comparable and traceable. In the past decades, quantum cascade lasers (QCL) have been developed to provide a high-intensity monochromatic mid- and far-IR light and used for high-throughput polarization IR imaging.^{21,26} Recently, an algorithm was theoretically proposed to determine the 3D orientation angle by concurrently analyzing the 2D-projected polarization anisotropy of a pair of orthogonal IR transition dipoles.²⁷ Later, the orthogonal-pair polarization IR (OPPIR) method was experimentally demonstrated²⁸ for imaging the 3D molecular orientations in spherulites of a poly(ϵ -caprolactone) film. In this paper, we advanced the OPPIR imaging method to study the structural change occurring upon mechanical deformation of the semicrystalline polymer film. The paper provides a statistical analysis of chain orientations before and after shear deformation and in-depth spectral deconvolution of vibrational modes into the crystalline and amorphous chains. Based on the newly accessible results, we discuss the polymer physics associated with shear deformation, including out-of-

Received: September 28, 2021

Revised: March 17, 2022

plane chain alignment and orientational relaxation in the shear-deformed polymer film.

MATERIALS AND METHODS

Sample Preparation. Poly(ϵ -caprolactone) (PCL, $M_n = 70,000$ – $90,000$, Aldrich) was dissolved in chloroform for a (3 mass %) solution. The solution was spin-cast onto a cover glass at 2000 rpm for 30 s. The film was annealed at 70 °C and cooled to room temperature, which was repeated three times. The PCL thin film was transferred to a CaF₂ window. A corner of the PCL film was sheared by pressing/spreading with a gently applied force with an edge of a glass slide. The thickness of the quiescent spherulite region was (5.5 ± 0.5) μm , and the thickness of the sheared region was (1.0 ± 0.1) μm .

Polarization IR Image Acquisition. The polarization-controlled hyperspectral IR microscopy system was described elsewhere.²⁸ (See Figure 1a for the schematic illustration.) Briefly, the PCL film was imaged with a wide-field QCL-IR microscope (Spero, Daylight Solutions, Inc., San Diego, USA). Linearly polarized incident light passed through an achromatic IR half-wave plate (XCN, Gooch & Housego) mounted to a computer-controlled rotation stage. The overall polarization performance of the system, including the achromatic half-wave plate, was tested by inserting a polarizer at the sample location (see Figure S1). The relative offset ($=T_{\min}/T_{\max}$), where T is the transmittance, was smaller than 0.02, and the phase angle variation was narrower than 2° over the entire reference polarizer image measured at 1500 cm⁻¹. The maximum relative offset was 0.03 over the entire wavelength range. A wide-field IR image was collected in transmission mode at each frequency while scanning the frequency from 1794 to 1000 cm⁻¹ with a 2 cm⁻¹ increment. An objective lens with 0.7 NA produced 650 μm field-of-view, 1.4 μm pixel size, 480 × 480 pixels, and diffraction-limited spatial resolution of approximately 5 μm . At a single location, 24 hyperspectral images were acquired as the achromatic waveplate was rotated to move by an 8° increment in a polarization angle over 180°. For the reference measurement, the sample stage was translated to image a blank area of a pristine portion of the CaF₂ substrate at each polarization angle. For a set of wide-field hyperspectral polarization images at a location, the total acquisition time for 398 frequency increments and 24 polarization steps was 44 min. The whole beam path from the laser to the detector inside the microscope enclosure was purged with dry nitrogen during image acquisition.

RESULTS AND DISCUSSION

Figure 1b shows the monomer structure of PCL, which was used to make a semicrystalline polymer film. A part of the spun-cast PCL film was sheared by pressing/spreading with a gently applied force with an edge of a glass slide, as displayed in Figure 1c. The low-magnification image of Figure 1d shows that the quiescent and the sheared regions are different in morphology. To investigate the difference in molecular orientation between the quiescent and the sheared regions, we focused on three adjacent rectangular areas, denoted as Q (quiescent), M (mixed), and S (sheared) at the boundary. Figure 1e–g shows the high-magnification images of the Q, M, and S regions, respectively, constructed with the mean absorbance over the entire frequency range. In the Q region, individual spherulite domains are identifiable by the boundaries and the nucleation centers. Despite shear deformation in the S region, the domains still remain recognizable as elongated traces along the shearing direction. The observed aspect ratio of the elongated domain traces is approximately five. This aspect ratio is similar to the separately measured thickness ratio between the quiescent region of (5.5 ± 0.5) μm thickness and the thinned sheared region of (1.0 ± 0.1) μm thickness, indicating that the Poisson contraction occurred in the film's normal direction.

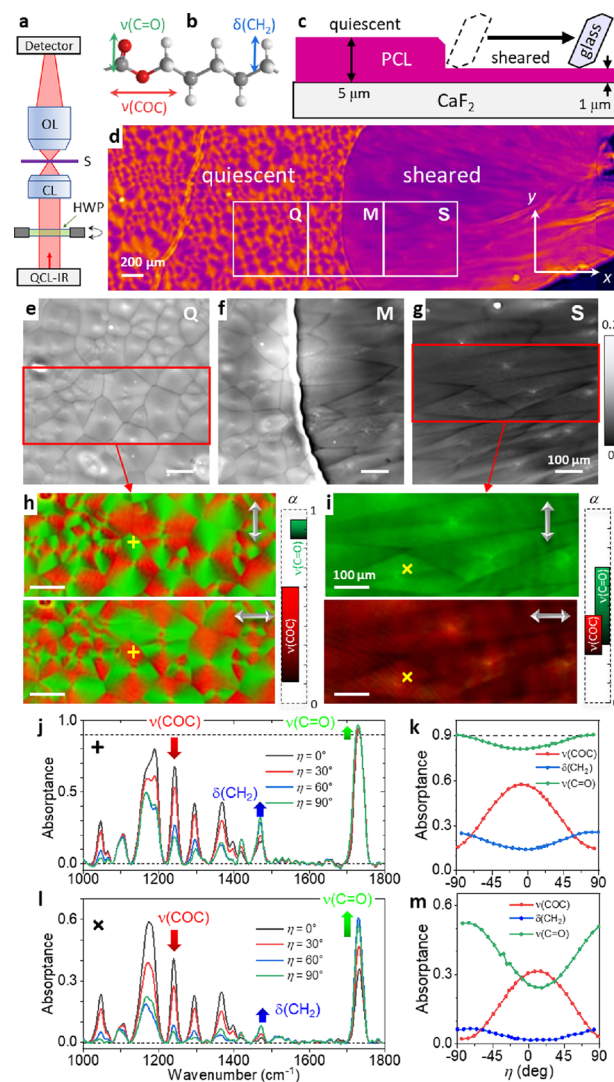


Figure 1. (a) Schematic illustration of the QCL-based wide-field polarization-controlled infrared microscope, where S denotes the sample; CL denotes the condenser lens; and OL denotes the objective lens. (b) Monomer structure of PCL and three representative vibrational modes. (c) Illustration of shearing the PCL film with the edge of a glass slide. (d) Large-area IR absorbance image of a partially shear-deformed PCL film at 1240 cm⁻¹. (e–g) Mean absorbance images over the entire scanning frequency range from 1000 to 1794 cm⁻¹ of the square sections labeled in (d) as Q (quiescent), M (mixed), and S (sheared) at the boundary. The frequency-averaged absorbance images were acquired by linearly polarized light along the vertical axis. Composite images of the enlarged part of (h) Q region and (i) S region, constructed by absorbances at 1244 cm⁻¹ ($\nu(\text{COC})$, red) and 1730 cm⁻¹ ($\nu(\text{C=O})$, green) by vertical and horizontal polarizations (the white arrows). The absorbance at each pixel was calculated from the baseline detrended absorbance spectrum. The vertically displaced scale bars on the right side of each composite image pair represent the absorbance scale used for the composite images. (j) Polarization-dependent absorbance spectra at the “+” mark in the Q region. (k) Polarization profiles of the absorbances measured at the frequencies corresponding to the $\nu(\text{COC})$ mode at 1244 cm⁻¹, the $\delta(\text{CH}_2)$ mode at 1470 cm⁻¹, and the $\nu(\text{C=O})$ mode at 1730 cm⁻¹ at the same location as (j). η denotes the polarization angle of the incident light from the x -axis. (l) Polarization-dependent absorbance spectra at the “x” mark in the S region. (m) Polarization profiles of the absorbances measured at the three frequencies at the same location as (l).

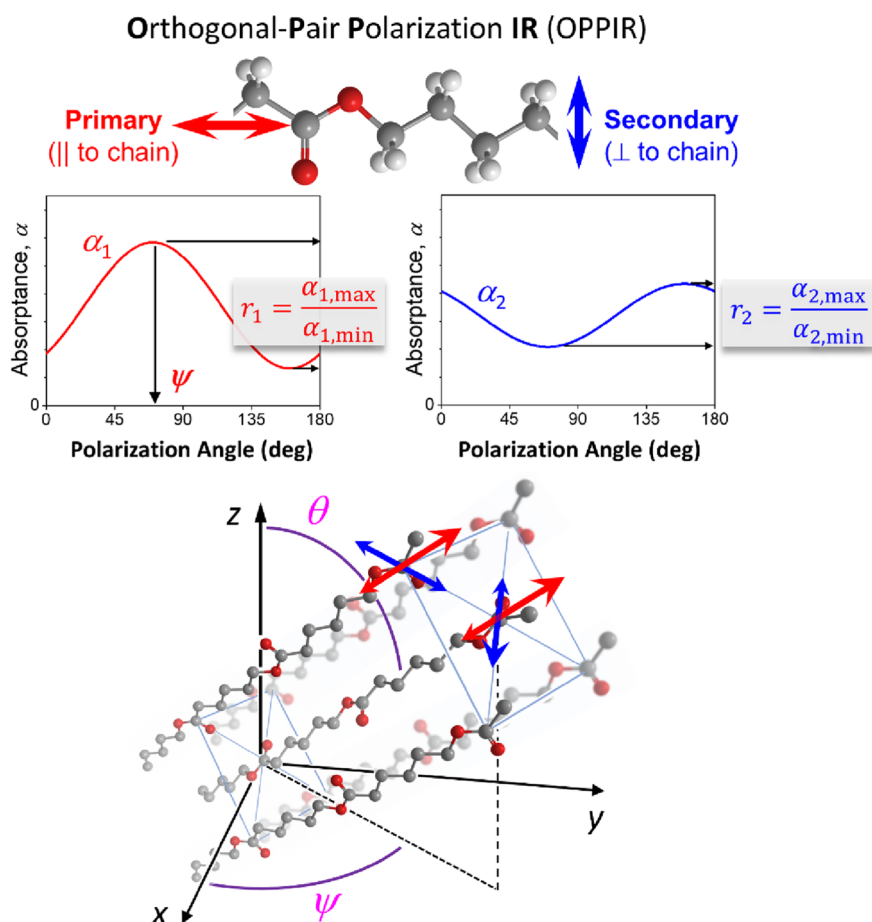


Figure 2. Schematic presentation of the OPPIR method to determine the 3D orientation angles and the order parameter. The transition dipole of the primary IR mode is parallel to the chain direction, and the transition dipole of the secondary mode is perpendicular to the chain direction. The IR absorbances (α_1 and α_2) of the two modes are measured as a function of polarization angle. The polarization anisotropies of the two modes (r_1 and r_2) are converted into $\langle \theta \rangle$ and $\langle P_2 \rangle$ with eqs 3 and 4. The phase angle of the primary mode (the black vertical arrow) is used to determine ψ . A unit cell of crystalline PCL consists of two groups of orientations. Their molecular planes (blue arrows) are oriented in two nearly orthogonal directions, while the main chains (red arrows) are parallel.

Figure 1h,i shows the composite images constructed by two specific frequencies corresponding to the C–O–C stretching mode, $\nu(\text{COC})$ at 1244 cm^{-1} , and the C=O stretching mode, $\nu(\text{C=O})$ at 1730 cm^{-1} . Unlike the frequency-averaged images of the Q region (Figure 1e), the composite image pair (Figure 1h) shows distinct anisotropic features: (a) a bow-tie pattern appears symmetrically around the nucleation center of a spherulite, (b) the bow-tie patterns are complementary between the $\nu(\text{C=O})$ (green) and the $\nu(\text{COC})$ (red), and (c) the entire pattern rotates by 90° between the vertical and horizontal polarization directions. These symmetrical features in the Q region strongly suggest that molecular alignment in a spherulite has a radial symmetry around the nucleation center. By contrast, the bow-tie pattern disappears in the S region (Figure 1i), suggesting that a significant change in molecular alignment occurred upon shear deformation despite the remaining trace of domains. The color contrast between the two polarization images of the S region indicates that the $\nu(\text{COC})$ mode (red) and the $\nu(\text{C=O})$ mode (green) align parallel and perpendicular to the shearing direction, respectively. For comparison, individual absorbance images of $\nu(\text{COC})$ at 1244 cm^{-1} , $\nu(\text{C=O})$ at 1730 cm^{-1} , and also $\delta(\text{CH}_2)$ at 1730 cm^{-1} are listed in Figure S2.

To determine the 3D orientation using polarization-dependent IR absorption, we use absorbance ($\alpha = 1 - T$) rather than absorbance ($A = -\log T$), where T is the transmittance.^{27,28} Figure 1j shows the absorbance spectra at various polarization angles at an image pixel in the Q region. Peaks at $<1400\text{ cm}^{-1}$, such as the $\nu(\text{COC})$ band, decrease as the polarization angle rotates from the x -axis ($\eta = 0^\circ$) to the y -axis ($\eta = 90^\circ$). Other peaks at $>1400\text{ cm}^{-1}$, such as the $\nu(\text{C=O})$ band and the $\delta(\text{CH}_2)$ band, increase from $\eta = 0$ to 90° . In Figure 1k, polarization-dependent absorbances of the three peaks exhibit that the $\nu(\text{COC})$ band is the maximum around $\eta = 0^\circ$ while the $\nu(\text{C=O})$ and the $\delta(\text{CH}_2)$ bands are the maxima near $\eta = 90^\circ$. The spectra and polarization profiles observed at a pixel in the S region (Figure 1l,m) also shows the out-of-phase polarization dependence between the $\nu(\text{COC})$ band and the other two bands of $\nu(\text{C=O})$ and $\delta(\text{CH}_2)$.

From both Q and S regions, the histograms of the phase angle difference ($\Delta\eta_{\text{max}}$) of the $\nu(\text{COC})$ – $\nu(\text{C=O})$ pair and the $\nu(\text{COC})$ – $\delta(\text{CH}_2)$ pair show a narrow distribution around 90° , as shown in Figure S3. Figure 1b shows that the direction of the $\nu(\text{COC})$ transition dipole is parallel to the main chain, and the $\nu(\text{C=O})$ and $\delta(\text{CH}_2)$ transition dipoles are perpendicular to the main chain. If all polymer chains are parallel aligned, also known as the oriented-gas model, $\Delta\eta_{\text{max}}$

can vary without restriction depending on the Euler angles of the chain orientation. However, the reported unit cell geometry of crystalline PCL consists of two differently oriented chains,^{29,30} different from the oriented-gas model. Their main chains are parallel to the *c*-axis of the unit cell, but their molecular planes are nearly orthogonal to each other. This unit cell geometry of orthogonal-facing chains is consistent with the observed $\Delta\eta_{\max} \approx 90^\circ$ (see the Supporting Information).

It is noted that the maximum absorbance of the $\nu(\text{C}=\text{O})$ band shown in Figure 1h,j is higher than 0.9 in the Q region due to the high absorption cross section and the film thickness. When the thickness is reduced by five times in the S region, the absorbance becomes lower than 0.9. The threshold of $\alpha = 0.9$ originates from the assumption used for analytical derivation of the OPPIR method and potential nonlinearity of the detection system response.²⁷ Therefore, we use the $\nu(\text{C}=\text{O})$ peak for 3D orientation analysis only in the S region. In the Q region, we will use the $\delta(\text{CH}_2)$ peak instead of the $\nu(\text{C}=\text{O})$ peak for analysis.

A scheme of the OPPIR algorithm is presented in Figure 2, and the detailed derivations of the OPPIR to determine the 3D orientation angles can be found elsewhere.^{27,28} Briefly, we assume that the orientational distribution function (ODF) of molecules within the probed volume is uniaxially symmetrical. Then, the 3D orientation direction of ODF can be described with the azimuthal angle (ψ) and the axial angle (θ), and the local orientational broadening can be represented by the order parameter from the second-order Legendre polynomials ($\langle P_2 \rangle$). From a prior knowledge of the relative geometry of transition dipole directions in a molecule or a unit cell, we identify an orthogonal pair of transition dipoles: one transition dipole parallel to the ODF symmetry axis is called the primary mode, and the other perpendicular to the symmetry axis is called the secondary mode.²⁷ For the orthogonal two-chain geometry discussed above, $\alpha(\eta)$ of both primary and secondary modes can be expressed with the shared parameters of the molecular symmetry axis (ψ , θ , and $\langle P_2 \rangle$).^{27,28}

$$\alpha_1(\eta) = \alpha_1^\circ \left\{ \langle P_2 \rangle \sin^2 \theta \cos^2(\eta - \psi) + \frac{1}{3}(1 - \langle P_2 \rangle) \right\} \quad (1)$$

$$\alpha_2(\eta) = \alpha_2^\circ \left\{ \frac{\langle P_2 \rangle}{2} [\sin^2 \theta \sin^2(\eta - \psi) + \cos^2 \theta] + \frac{1}{3}(1 - \langle P_2 \rangle) \right\} \quad (2)$$

where $\alpha_{1,2}^\circ$ is a polarization-independent parameter dependent on the sample density and the absorption cross section. From eq 1, ψ can be directly determined from the phase angle of $\alpha_1(\eta)$. Using polarization anisotropy defined for the primary and the secondary modes, respectively, as $r_1 \equiv (\alpha_{1,\max}/\alpha_{1,\min})$ and $r_2 \equiv (\alpha_{2,\max}/\alpha_{2,\min})$, we can determine $\langle P_2 \rangle$ and $\sin^2 \theta$ with

$$\langle P_2 \rangle = \frac{r_1 r_2 - 3r_2 + 2}{r_1 r_2 - 1} \quad (3)$$

$$\sin^2 \theta = \frac{r_1 r_2 - r_1 - r_2 + 1}{r_1 r_2 - 3r_2 + 2} \quad (4)$$

A few notable features of the OPPIR methods are (1) a single value of $\sin^2 \theta$ from eq 4 produces two indistinguishable values of $\pm\theta$; (2) the absorbance measured in the transmission mode reflects the averaged orientation of the

molecules within the imaging volume that the IR beam passes through; and (3) the OPPIR analysis does not require separate measurements of sample thickness, density, or absolute absorption cross section because the ratios, r_1 and r_2 , used in eqs 3 and 4 are dimensionless ratios.

We use the OPPIR algorithm to determine ψ , $|\theta|$, and $\langle P_2 \rangle$ at each image pixel independently and construct their images. First, the 3D orientation angles and the order parameter of the Q region in Figure 3a,d,g are reproduced from the earlier

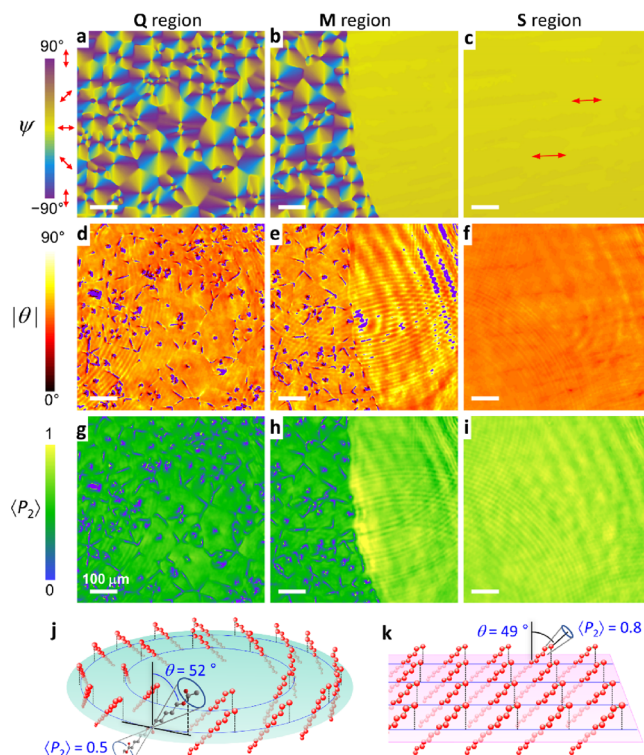


Figure 3. 3D orientation maps calculated from Q, M, and S regions using the OPPIR method. (a–c) Azimuthal angle (ψ) images determined by the polarization angle corresponding to $\alpha_{1,\max}$. (d–f) Axial angle ($|\theta|$) images calculated with eq 4. Image pixels outside the range of $0 \leq \sin^2 \theta \leq 1$ are colored as violet. (g–i) Order parameter ($\langle P_2 \rangle$) images calculated by eq 3. Image pixels outside the range $0 \leq \langle P_2 \rangle \leq 1$ are colored as violet. (j) Illustration of chain orientations inside a spherulite in the Q region. The cone represents orientational broadening for $\langle P_2 \rangle$. (k) Illustration of chain orientations in the S region. The figures of (a, d, g, j) from the Q region are the reprocessed OPPIR results using the identical original data of ref 28.

results.²⁸ Briefly, the ψ image of Figure 3a shows that PCL chain projections to the polarization plane are symmetrically aligned tangential to circumferences from the nucleation center of each spherulite. This result of the tangential alignment of the azimuthal angles is similar to the earlier report on 2D-projected polarization IR images of nonbanded PCL spherulites.²² The $|\theta|$ image in Figure 3d appears nearly uniform overall except for the nucleation centers and the spherulite boundaries, where the ODF are considered to be non-uniaxial and out of the scope of the OPPIR algorithm. Similar to the $|\theta|$ image, the $\langle P_2 \rangle$ image in Figure 3g looks flat over the crystal growth region except for the outlier pixels. The values of ψ , $|\theta|$, and $\langle P_2 \rangle$ from all pixels (480×480 pixels) in the Q region are summarized in the histograms shown in Figure 4a–c. Unlike the isotropically distributed ψ , the

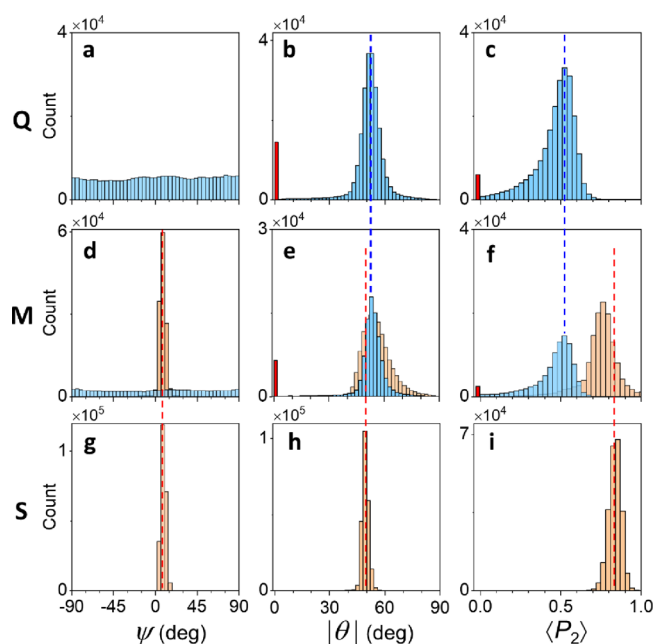


Figure 4. Histograms of the ψ , $|\theta|$, and $\langle P_2 \rangle$ values in **Q**, **M**, and **S** regions. In the **M** region, the image pixels corresponding to the quiescent (light blue) and the sheared (light orange) areas are separately counted. In all regions, the $\nu(\text{COC})$ peak was used as the primary mode. The $\delta(\text{CH}_2)$ peak was used as the secondary mode for the **Q** and **M** regions, while the $\nu(\text{C=O})$ peak was used as the secondary mode for the **S** region.

distribution of $|\theta|$ is narrow with the median value of 52° and the full-width-half-maximum (fwhm) of 8° . Using the tangential ψ and the median values of $|\theta|$, the chain orientation in a spherulite is illustrated in Figure 3j.

The molecular alignment in the **S** region is quite different from that in the **Q** region. The homogeneous ψ image in Figure 3c and the narrow distribution in the ψ histogram in Figure 4g indicate that the projections of polymer chains are aligned along the shear direction (\approx the x -axis). Similar to the ψ image, the $|\theta|$ image in Figure 3f looks homogeneous, and the $|\theta|$ histogram in Figure 4h shows a narrow distribution. However, the median value of $|\theta|$ indicates that the chains are not aligned parallel to the shearing direction but deviated by 38° ($|\theta| = 52^\circ$) from the film plane. From the median values of ψ and $|\theta|$ of the **S** region, the orientation of PCL chains in the sheared film is illustrated in Figure 3k. This out-of-plane orientation in the **S** region will be discussed later in connection with orientational relaxation. Similar to the ψ and $|\theta|$ images, the $\langle P_2 \rangle$ image of the **S** region in Figure 3i also does not indicate any memory of the spherulite domains, although the traces appear in the absorption image in Figure 1g. The $\langle P_2 \rangle$ histogram in Figure 4i shows that shear deformation increased the median $\langle P_2 \rangle$ from 0.51 (**Q** region) to 0.84 (**S** region), indicating that polymer chains become more tightly aligned around the mean orientation of the local ODF.

The **M** region can be divided into two distinct areas: quiescent (**Q**-like) and shear-deformed (**S**-like) areas. The OPPIR analysis for **M** region employed the $\delta(\text{CH}_2)$ peak as the secondary mode because the absorbance of the $\nu(\text{C=O})$ peak is too high in the **Q**-like area. However, the $\delta(\text{CH}_2)$ peak is more susceptible to spectral interference than the highly absorbing $\nu(\text{C=O})$ peak. Spectral interference, which is observed as the fringes in Figure 3, is caused by the light

interferences reflected from multiple interfaces of the film and the substrate.^{31–33} Since interference depends on the wavelength and the gap between reflecting surfaces, the fringes occur in both the spectrum and the space, making it difficult to remove with a simple numerical method. Overall, the 3D orientation results of the **Q**-like and **S**-like areas in the **M** region can be considered as the continuation of the neighboring **Q** and **S** regions, respectively. The sharp transition ($<10 \mu\text{m}$) from **Q**-like to **S**-like areas suggests that the PCL structural deformation occurred only where the shearing force was applied. The clear division of the **M** region into the **Q**-like and **S**-like orientations can be found in the histograms in Figure 4d–f. The distributions of the image pixels in the **Q**-like area (the light blue bars) are similar to the corresponding distributions of the **Q** region (Figure 4a–c), and the distributions of the **S**-like area (the light orange bars) are similar to the corresponding distributions of the **S** region (Figure 4g–i). It is noted that the $|\theta|$ and $\langle P_2 \rangle$ distributions of the **S**-like area in the **M** region are shifted from and broader than the corresponding distributions of the **S** region because of the different peaks used for the secondary mode.

Because the sample was sheared above PCL's glass transition temperature (209 K),³⁴ the molten entangled amorphous polymer chains, strain transmitters, and crystal lamellae in spherulites are expected to realign so that the projection of the chains to the film surface is parallel to the stretching direction. Because of the low shear rate, the lamellae are primarily expected to rotate. However, they can also undergo the increasingly severe deformation mechanisms of crystal slip, crystal fragmentation, and chain pullout, with the latter expected to result in a decrease in crystallinity.^{35,36} Regardless, when the shear force stretches the PCL thin film, the individual polymer chains are translated far from the original locations and later become stabilized or recrystallized. Unlike stretching in a free-standing polymer film, the stretching by shearing breaks the symmetry in the normal direction of the film, which may cause the mean chain orientation to deviate from the plane. A different stretching condition could have resulted in different orientation angles and order parameters.

In Figure 3, some image pixels near spherulite centers and boundaries in the **Q** region have unreal values of θ and $\langle P_2 \rangle$ from eqs 3 and 4. Multiple possible origins of the failing OPPIR calculation were discussed in the earlier paper.²⁸ Among them, non-uniaxial orientation distributions showed consistent results with simulations performed with two coexisting orientation distributions of nonparallel azimuthal angles. In contrast to the domain-structured **Q** region, there are no pixels with unreal values of θ and $\langle P_2 \rangle$ in the **S** region, which suggests that the shearing deformation makes the molecular orientation more uniform macroscopically. The macroscopic (at a longer length scale than the image resolution) homogeneity is consistent with the narrow distribution of $\langle P_2 \rangle$ in Figure 4i. The orientational homogeneity enhanced by shearing deformation can also be found microscopically (smaller than the image resolution) because the mean $\langle P_2 \rangle$ is higher in the **S** region than in the **Q** region.

Previous IR spectroscopic studies of PCL showed that several IR peaks could be deconvoluted into subbands corresponding to the crystalline and amorphous configurations.^{37,38} We focus on the $\nu(\text{C=O})$ peak and $\nu(\text{COC})$ peak, which we used for the OPPIR for the **S** region. We analyze the $\nu(\text{C=O})$ peak and the $\nu(\text{COC})$ peak in the ensemble spectra as a function of polarization angle by two-dimensional

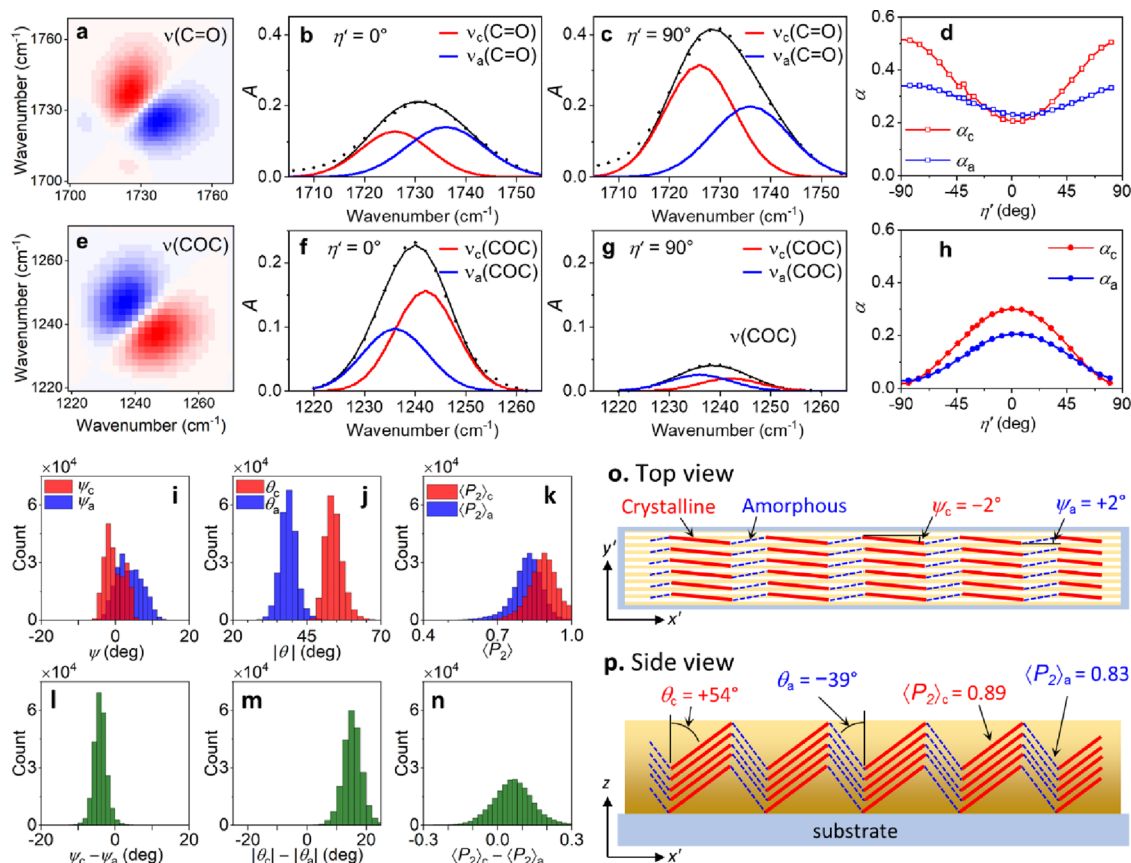


Figure 5. 3D orientations of crystalline and amorphous chains in the S region. (a) Asynchronous 2DCOS map of the $\nu(\text{C}=\text{O})$ peak with respect to the polarization angle. (b, c) Absorbance spectra (dotted) ensemble-averaged over the S region at two representative polarization angles for the $\nu(\text{C}=\text{O})$ mode. Each peak is fitted with two Gaussian functions: the red curve, centering at 1726 cm^{-1} (fwhm = 16 cm^{-1}), corresponds to the crystalline phase; and the blue curve, at 1736 cm^{-1} (fwhm = 18 cm^{-1}), corresponds to the amorphous phase. (d) Ensemble-averaged absorbance of the crystalline and the amorphous functions of the $\nu(\text{C}=\text{O})$ mode as a function of η' . (e) Asynchronous 2DCOS map of the $\nu(\text{COC})$ peak. (f, g) Ensemble-averaged absorbance spectra (dotted) for the $\nu(\text{COC})$ mode at two different polarization angles. Each peak is fitted with two Gaussian functions: the red curve, centering at 1242 cm^{-1} (fwhm = 14 cm^{-1}), corresponds to the crystalline phase; and the blue curve, at 1236 cm^{-1} (fwhm = 15 cm^{-1}), corresponds to the amorphous phase. (h) Ensemble-averaged absorbance of the crystalline and the amorphous functions of the $\nu(\text{COC})$ mode as a function of η' . (i–k) Histograms of ψ , $|\theta|$, and $\langle P_2 \rangle$, respectively, of the crystalline and the amorphous chains. (l–n) Histograms of $(\psi_c - \psi_a)$, $(|\theta_c| - |\theta_a|)$, and $(\langle P_2 \rangle_c - \langle P_2 \rangle_a)$, respectively. (o) Top view and (p) side view of crystalline and the amorphous chains coexisting in the S region. The ψ , θ , and $\langle P_2 \rangle$ values of each configuration are taken from the median values in the histograms of (i–k).

correlation spectroscopy (2DCOS), which can be used to resolve peaks without a priori knowledge of the position and the shape of underlying peaks.^{39,40} Two unambiguous spectral components in the 2DCOS asynchronous maps of Figure 5a,e indicate that two embedded subcomponents respond to the rotating polarization angle differently. Earlier IR measurements of PCL^{38,41} show that the $\nu(\text{C}=\text{O})$ peak downshifts, and the $\nu(\text{COC})$ peak upshifts when cooled from the melt state to the semicrystalline state. Therefore, we deconvoluted the $\nu(\text{C}=\text{O})$ and $\nu(\text{COC})$ peaks with two underlying components to determine the chain orientations in the crystalline and the amorphous configurations separately. Figure 5b,c shows that the $\nu(\text{C}=\text{O})$ spectra ensemble-averaged over the S region at two polarization angles can be deconvoluted into two Gaussian functions with center positions and widths unvarying with respect to the polarization angle. For the peak fitting, we used absorbance spectra instead of absorbance because absorbance of multiple components can be expressed as the sum of the absorbances of the subcomponents. The underlying Gaussian function centered at 1726 cm^{-1} corresponds to the IR absorption of the crystalline configuration, $\nu_c(\text{C}=\text{O})$, while the other function centered at 1736 cm^{-1} corresponds to that

of the amorphous configuration, $\nu_a(\text{C}=\text{O})$. Similarly, the $\nu(\text{COC})$ peak is deconvoluted into two Gaussian functions, shown in Figure 4f,g. The Gaussian function centered at 1242 cm^{-1} corresponds to the crystalline configuration, $\nu_c(\text{COC})$, and the function at 1236 cm^{-1} corresponds to the amorphous configuration, $\nu_a(\text{COC})$.

The ratio of the underlying peak areas from IR and Raman has been used to measure the crystallinity of polymers non-invasively.^{42–44} Similarly, we define IR crystallinity as $\chi_{\text{IR}} \equiv A_c / (A_c + A_a)$, where A_c and A_a are the areas of the crystalline and amorphous components, respectively. When we used the polarization-angle-averaged and ensemble-averaged spectrum to calculate χ_{IR} , the results are $\langle \chi_{\text{IR}}(\text{C}=\text{O}) \rangle = (56 \pm 3)\%$ and $\langle \chi_{\text{IR}}(\text{COC}) \rangle = (58 \pm 5)\%$. The uncertainties in χ_{IR} indicate the standard deviation calculated from five different parameters that produce visually acceptable fitting results (Table S1). These spectrally determined crystallinities are similar to reported values for similarly prepared PCL films.^{38,44,45} We compare the IR crystallinities with the thermodynamic crystallinity, which we measured using differential scanning calorimetry (DSC) on a similarly sheared piece from an identically prepared film (Figure S4). The measured

thermodynamic mass fraction crystallinity, $\chi_{\text{DSC}} = (49 \pm 3)\%$, where the uncertainty was estimated from previous measurements of similar samples, is consistent with the χ_{IR} values obtained from this work.

Since both the primary and the secondary modes in the S region can be spectrally deconvoluted into the crystalline and the amorphous configurations, we determine the 3D orientations of the crystalline and the amorphous chains separately. The mean absorptances, α_c and α_a , of the crystalline and the amorphous chains, respectively, are calculated and plotted as a function of polarization angle in Figure 5d,h. We determine the 3D orientation angles and the order parameter using the OPPIR algorithm for the crystalline and the amorphous components separately at each image pixel in the S region.

Figure 5i–k shows the histograms of ψ , $|\theta|$, and $\langle P_2 \rangle$ of the crystalline and the amorphous chains. In all histograms, the crystalline and the amorphous chains show similar widths but shifted distributions. The distributions of ψ_c and ψ_a in Figure 5i are separated by 4.0° , which is consistent with the median value of the $(\psi_c - \psi_a)$ distribution in Figure 5l. Interestingly, the $(\psi_c - \psi_a)$ distribution (fwhm = 3.2°) in Figure 5l is much narrower than the individual ψ_c (fwhm = 7.1°) and ψ_a distributions (fwhm = 9.1°) in Figure 4i. The distributions of $|\theta_c|$ and $|\theta_a|$ in Figure 5j are more clearly separated than those of ψ_c and ψ_a in Figure 5i. $|\theta_c| = 54^\circ$ is larger than $|\theta_a| = 39^\circ$. Similar to the $(\psi_c - \psi_a)$ distribution, the $(|\theta_c| - |\theta_a|)$ distribution in Figure 5m exhibits a smaller fwhm ($=5.5^\circ$) than the individual fwhms of 6.2 and 6.5° for $|\theta_c|$ and $|\theta_a|$, respectively. Overall, although the crystalline and the amorphous chains are differently oriented in both ψ and $|\theta|$, the two types of chains are locally correlated within the probed focus volume than the large area heterogeneity in the S region. Figure 5k shows that $\langle P_2 \rangle_c$ is slightly higher than $\langle P_2 \rangle_a$, indicating that the ODF of the crystalline chains is narrower than the ODF of the amorphous chains within the focus volume. Unlike the narrow distributions of $(\psi_c - \psi_a)$ and $(|\theta_c| - |\theta_a|)$, the distribution of the $(\langle P_2 \rangle_c - \langle P_2 \rangle_a)$ in Figure 5n is not narrower than the individual distributions, indicating that the local orientational broadenings are not as correlated as the local orientation directions of the crystalline and the amorphous chains.

Figure 5o illustrates the top view of the orientations of crystalline and amorphous chains and displays azimuthal zigzags by 4° between ψ_c and ψ_a . A more noteworthy difference between the crystalline and the amorphous chain orientations can be found in the side view of Figure 5p. From $|\theta_c| = 54^\circ$ and $|\theta_a| = 39^\circ$, multiple combinations of θ_c and θ_a are possible. If all existing θ_c and θ_a have the same signs, the overall chain direction including both crystalline and amorphous chains will either go upward ($\theta_c = +54^\circ$; $\theta_a = +39^\circ$) or downward ($\theta_c = -54^\circ$; $\theta_a = -39^\circ$). Alternatively, if θ_c and θ_a may have the opposite signs, as presented in Figure 5p, the overall chain direction will become nearly parallel to the shear direction.

We consider the transient alignment of PCL chains during shear in connection with the final alignment after relaxation to the nonspherulitic semicrystalline phase. Because the ψ distribution in the sheared film became conspicuously narrower compared to the quiescent spherulite region, we can assume that the deformation force made the whole chains aligned along the shear direction while being sheared. During relaxation, some chains crystallized while the others remained

in the amorphous configuration. At the same time, the crystalline and the amorphous chains were reoriented, deviating from the shear direction. If the reorientation during relaxation was local, the final overall chain orientation should not be very different from the shear direction, which would explain the opposite signs for $(\theta_c$ vs $\theta_a)$ and $(\psi_c$ vs $\psi_a)$. Interestingly, the chain reorientation during relaxation occurred primarily along the out-of-plane direction (θ) rather than the in-plane direction (ψ), which indicates that the relaxation results in more film thickening than film widening. The OPPIR of the spectrally resolved peaks allows us to understand the detailed molecular orientations of the crystalline and amorphous chains and the shear-relaxation mechanism.

The crystalline phase consists of highly ordered lamellae, where polymer chains are tightly packed and folded. Depending on crystallization conditions and molecular structures, the lamellae form spherulites or loosely connected parallel stacks. The arrangement and geometry of the lamellae significantly affect the macroscopic properties of the bulk polymer. Based on the chain-observed orientations, we discuss lamella orientations in the Q and S regions. The simplest and broadly adopted model is the “normal-chain” model,⁴⁶ where polymer chains are aligned normal to the lamella plane. In this model, the orientation of lamella planes is unambiguously determined by the chain orientation. Figure 55a illustrates a stack of lamellae and polymer chains in a spherulite for the normal-chain model, where the lamellae are tilted by θ . In a sheared film, the lamellae are leaning toward or away from the shear direction. An alternative model is the “tilted-chain” model, where the polymer chains are tilted by a certain angle to the lamella plane.^{47,48} A couple of lamella schemes based on the tilted-chain model can be found in Figure 55b. Although the absolute orientation of lamellae and the relative chain tilting will require additional independent characterization methods, these 3D chain orientation results can provide a critical piece of information about the hierarchical polymer structure and the mechanisms behind the crystal growth in a spherulite and the recrystallization after mechanical deformations.

CONCLUSIONS

We have demonstrated that a new optical imaging technique based on the OPPIR can determine the 3D angles and the order parameter of the molecular orientation at each image pixel from the polarization-dependent absorption of two orthogonal IR modes. The 3D orientation maps of polymer chains in a quiescent region and a shear-deformed region of a PCL film were constructed from hyperspectral data measured using a high-throughput polarization-controlled wide-field QCL-IR microscope. We compared the images of the 3D angles and the order parameter of the polymer chain orientation before and after shearing. The newly revealed molecular information allowed us to discuss the mechanisms of mechanical deformation and configurational relaxation occurring in hierarchical molecular structures. This versatile imaging approach is a substantial advancement from existing, restrictive tomographic techniques and is, thus, capable of broadly advancing the understanding of the structure–property relations in natural and synthetic materials.

■ ASSOCIATED CONTENT

SI Supporting Information

The Supporting Information is available free of charge at <https://pubs.acs.org/doi/10.1021/acs.macromol.1c02036>.

Description of the baseline detrending process of absorbance spectra; equations for the orthogonal-pair polarization IR (OPPIR) analysis; effect of non-B Beer–Lambert distortion on the OPPIR results; polarimetric performance of the achromatic half-wave plate (Figure S1); absorbance images of the **Q** region by three frequencies (Figure S2); histograms of $\Delta\eta_{\max}$ for **Q** and **S** regions (Figure S3); differential scanning calorimetry (DSC) traces for the sheared and unsheared PCL samples (Figure S4); schematic illustrations of lamella stacking (Figure S5); raw and detrended spectra (Figure S6); effect of the wave-optics correction (Figure S7); and IR crystallinity calculated by peak fitting (Table S1) (PDF)

■ AUTHOR INFORMATION

Corresponding Author

Young Jong Lee – Biosystems and Biomaterials Division, National Institute of Standards and Technology, Gaithersburg, Maryland 20899, United States; orcid.org/0000-0001-7754-3001; Email: youngjong.lee@nist.gov

Authors

Shuyu Xu – Biosystems and Biomaterials Division, National Institute of Standards and Technology, Gaithersburg, Maryland 20899, United States; orcid.org/0000-0001-6313-3773

Chad R. Snyder – Materials Science and Engineering Division, National Institute of Standards and Technology, Gaithersburg, Maryland 20899, United States; orcid.org/0000-0002-2916-9809

Jeremy Rowlette – DRS Daylight Solutions, San Diego, California 92127, United States

Complete contact information is available at:

<https://pubs.acs.org/doi/10.1021/acs.macromol.1c02036>

Author Contributions

Y.J.L. and J.A.R. performed the polarization QCL-IR imaging. C.R.S. performed the DSC measurements. S.X. and Y.J.L. analyzed the hyperspectral images with the OPPIR method. S.X. and Y.J.L. wrote the paper. Y.J.L. supervised the project. The manuscript was written through the contributions of all authors.

Notes

The authors declare no competing financial interest. Certain commercial equipment, instruments, or materials are identified in this paper to foster understanding. Such identification does not imply endorsement by NIST, nor does it imply that the materials or equipment identified are necessarily the best available for the purpose. Official contribution of NIST; not subject to copyright in the United States.

■ ACKNOWLEDGMENTS

We thank Desu Chen and Sumona Sarkar for preparing the PCL film; Lee Richter for measuring the film thickness with an ellipsometer; and Kern Lee for illustrating the cover art.

■ REFERENCES

- (1) Cranford, S. W.; Tarakanova, A.; Pugno, N. M.; Buehler, M. J. Nonlinear Material Behaviour of Spider Silk Yields Robust Webs. *Nature* **2012**, *482*, 72–76.
- (2) Malkin, A. Y. Shear-Induced Transitions in Colloidal and Polymeric Liquids. *Adv. Colloid Interface Sci.* **2021**, *290*, No. 102381.
- (3) Luo, C.; Atvars, T. D. Z.; Meakin, P.; Hill, A. J.; Weiss, R. G. Determination of Initial and Long-Term Microstructure Changes in Ultrahigh Molecular Weight Polyethylene Induced by Drawing Neat and Pyrenyl Modified Films. *J. Am. Chem. Soc.* **2003**, *125*, 11879–11892.
- (4) Wenk, H.-R.; Van Houtte, P. Texture and Anisotropy. *Rep. Prog. Phys.* **2004**, *67*, 1367–1428.
- (5) Lafrance, C. P.; Pezolet, M.; Prud'homme, R. E. Study of the Distribution of Molecular Orientation in Highly Oriented Polyethylene by X-Ray Diffraction. *Macromolecules* **1991**, *24*, 4948–4956.
- (6) Kuhlmann, M.; Feldkamp, J. M.; Patommel, J.; Roth, S. V.; Timmann, A.; Gehrke, R.; Müller-Buschbaum, P.; Schroer, C. G. Grazing Incidence Small-Angle X-Ray Scattering Microtomography Demonstrated on a Self-Ordered Dried Drop of Nanoparticles. *Langmuir* **2009**, *25*, 7241–7243.
- (7) Liu, H. H.; Schmidt, S.; Poulsen, H. F.; Godfrey, A.; Liu, Z. Q.; Sharon, J. A.; Huang, X. Three-Dimensional Orientation Mapping in the Transmission Electron Microscope. *Science* **2011**, *332*, 833–834.
- (8) Eggeeman, A. S.; Krakow, R.; Midgley, P. A. Scanning Precession Electron Tomography for Three-Dimensional Nanoscale Orientation Imaging and Crystallographic Analysis. *Nat. Commun.* **2015**, *6*, 7267.
- (9) Koenig, J. L.; Cornell, S. W.; Witenhafer, D. E. Infrared Technique for the Measurement of Structural Changes during the Orientation Process in Polymers. *J. Polym. Sci., Part A: Polym. Phys.* **1967**, *5*, 301–313.
- (10) Kossack, W.; Schulz, M.; Thurn-Albrecht, T.; Reinmuth, J.; Skokow, V.; Kremer, F. Temperature-Dependent IR-Transition Moment Orientational Analysis Applied to Thin Supported Films of Poly- ϵ -Caprolactone. *Soft Matter* **2017**, *13*, 9211–9219.
- (11) Shioya, N.; Tomita, K.; Shimoaka, T.; Hasegawa, T. Second Generation of Multiple-Angle Incidence Resolution Spectrometry. *J. Phys. Chem. A* **2019**, *123*, 7177–7183.
- (12) Chang, W.-S.; Ha, J. W.; Slaughter, L. S.; Link, S. Plasmonic Nanorod Absorbers as Orientation Sensors. *Proc. Natl. Acad. Sci.* **2010**, *107*, 2781–2786.
- (13) Prokhorov, V. V.; Pozin, S. I.; Perelygina, O. M.; Mal'Tsev, E. I. Crystallography and Molecular Arrangement of Polymorphic Monolayer J-Aggregates of a Cyanine Dye: Multiangle Polarized Light Fluorescence Optical Microscopy Study. *Langmuir* **2018**, *34*, 4803–4810.
- (14) Plotnikov, S. V.; Millard, A. C.; Campagnola, P. J.; Mohler, W. A. Characterization of the Myosin-Based Source for Second-Harmonic Generation from Muscle Sarcomeres. *Biophys. J.* **2006**, *90*, 693–703.
- (15) Lee, Y. J.; Snyder, C. R.; Forster, A. M.; Cicerone, M. T.; Wu, W. L. Imaging the Molecular Structure of Polyethylene Blends with Broadband Coherent Raman Microscopy. *ACS Macro Lett.* **2012**, *1*, 1347–1351.
- (16) Cleff, C.; Gasecka, A.; Ferrand, P.; Rigneault, H.; Brasselet, S.; Duboisset, J. Direct Imaging of Molecular Symmetry by Coherent Anti-Stokes Raman Scattering. *Nat. Commun.* **2016**, *7*, 11562.
- (17) Kennedy, A. P.; Sutcliffe, J.; Cheng, J.-X. Molecular Composition and Orientation in Myelin Figures Characterized by Coherent Anti-Stokes Raman Scattering Microscopy. *Langmuir* **2005**, *21*, 6478–6486.
- (18) Masic, A.; Bertinetti, L.; Schuetz, R.; Galvis, L.; Timofeeva, N.; Dunlop, J. W. C.; Seto, J.; Hartmann, M. A.; Fratzl, P. Observations of Multiscale, Stress-Induced Changes of Collagen Orientation in Tendon by Polarized Raman Spectroscopy. *Biomacromolecules* **2011**, *12*, 3989–3996.
- (19) Koziol, P.; Liberda, D.; Kwiatek, W. M.; Wrobel, T. P. Macromolecular Orientation in Biological Tissues Using a Four-

Polarization Method in FT-IR Imaging. *Anal. Chem.* **2020**, *92*, 13313–13318.

(20) Ryu, M.; Balčytis, A.; Wang, X.; Vongsivut, J.; Hikima, Y.; Li, J.; Tobin, M. J.; Juodkazis, S.; Morikawa, J. Orientational Mapping Augmented Sub-Wavelength Hyper-Spectral Imaging of Silk. *Sci. Rep.* **2017**, *7*, 7419.

(21) Mukherjee, P.; Ghosh, A.; Spegazzini, N.; Lamborn, M. J.; Monwar, M. M.; DesLauriers, P. J.; Bhargava, R. Relating Post-Yield Mechanical Behavior in Polyethylenes to Spatially Varying Molecular Deformation Using Infrared Spectroscopic Imaging: Homopolymers. *Macromolecules* **2018**, *51*, 3836–3844.

(22) Kossack, W.; Kremer, F. Banded Spherulites and Twisting Lamellae in Poly- ϵ -Caprolactone. *Colloid Polym. Sci.* **2019**, *297*, 771–779.

(23) Hikima, Y.; Morikawa, J.; Hashimoto, T. Wavenumber Dependence of FT-IR Image of Molecular Orientation in Banded Spherulites of Poly(3-Hydroxybutyrate) and Poly(L-Lactic Acid). *Macromolecules* **2013**, *46*, 1582–1590.

(24) Citra, M. J.; Chase, D. B.; Ikeda, R. M.; Gardner, K. H. Molecular Orientation of High-Density Polyethylene Fibers Characterized By Polarized Raman-Spectroscopy. *Macromolecules* **1995**, *28*, 4007–4012.

(25) Hikima, Y.; Morikawa, J.; Hashimoto, T. FT-IR Image Processing Algorithms for In-Plane Orientation Function and Azimuth Angle of Uniaxially Drawn Polyethylene Composite Film. *Macromolecules* **2011**, *44*, 3950–3957.

(26) Wrobel, T. P.; Mukherjee, P.; Bhargava, R. Rapid Visualization of Macromolecular Orientation by Discrete Frequency Mid-Infrared Spectroscopic Imaging. *Analyst* **2017**, *142*, 75–79.

(27) Lee, Y. J. Concurrent Polarization IR Analysis to Determine the 3D Angles and the Order Parameter for Molecular Orientation Imaging. *Opt. Express* **2018**, *26*, 24577–24590.

(28) Xu, S.; Rowlette, J.; Lee, Y. J. Imaging 3D Molecular Orientation by Orthogonal-Pair Polarization IR Microscopy. *Opt. Express* **2022**, *30*, 8436–8447.

(29) Chatani, Y.; Okita, Y.; Tadokoro, H.; Yamashita, Y. Structural Studies of Polyesters. III. Crystal Structure of Poly- ϵ -Caprolactone. *Polym. J.* **1970**, *1*, 555–562.

(30) Funaki, C.; Yamamoto, S.; Hoshina, H.; Ozaki, Y.; Sato, H. Three Different Kinds of Weak C-H \cdots O=C Inter- and Intramolecular Interactions in Poly(ϵ -Caprolactone) Studied by Using Terahertz Spectroscopy, Infrared Spectroscopy and Quantum Chemical Calculations. *Polymer* **2018**, *137*, 245–254.

(31) Schönals, A.; Kröger-Lui, N.; Pucci, A.; Petrich, W. On the Role of Interference in Laser-Based Mid-Infrared Widefield Microspectroscopy. *J. Biophotonics* **2018**, *11*, No. e201800015.

(32) Feng, S.; Zuo, C.; Hu, Y.; Li, Y.; Chen, Q. Deep-Learning-Based Fringe-Pattern Analysis with Uncertainty Estimation. *Optica* **2021**, *8*, 1507–1510.

(33) Azarfar, G.; Aboulzadeh, E.; Walter, N. M.; Ratti, S.; Olivieri, C.; Norici, A.; Nasse, M.; Kohler, A.; Giordano, M.; Hirschmugl, C. J. Estimating and Correcting Interference Fringes in Infrared Spectra in Infrared Hyperspectral Imaging. *Analyst* **2018**, *143*, 4674–4683.

(34) Gaur, U.; Lau, S. F.; Wunderlich, B. B.; Wunderlich, B. Heat Capacity and Other Thermodynamic Properties of Linear Macromolecules. VIII. Polyesters and Polyamides. *J. Phys. Chem. Ref. Data* **1983**, *12*, 65–89.

(35) Lee, S. Y.; Bassett, D. C.; Olley, R. H. Lamellar Deformation and Its Variation in Drawn Isolated Polyethylene Spherulites. *Polymer* **2003**, *44*, 5961–5967.

(36) Séguéla, R. On the Natural Draw Ratio of Semi-Crystalline Polymers: Review of the Mechanical, Physical and Molecular Aspects. *Macromol. Mater. Eng.* **2007**, *292*, 235–244.

(37) Mallapragada, S. K.; Narasimhan, B. Infrared Spectroscopy in Analysis of Polymer Crystallinity. In *Encyclopedia of Analytical Chemistry*; John Wiley & Sons, Ltd: Chichester, UK, 2006; pp. 1–14.

(38) He, Y.; Inoue, Y. Novel FTIR Method for Determining the Crystallinity of Poly(ϵ -Caprolactone). *Polym. Int.* **2000**, *49*, 623–626.

(39) Noda, I.; Ozaki, Y. *Two-Dimensional Correlation Spectroscopy*; Wiley & Sons: Chichester, West Sussex, 2004.

(40) Jin, Y.; Kotula, A. P.; Hight Walker, A. R.; Migler, K. B.; Lee, Y. J. Phase-Specific Raman Analysis of n-Alkane Melting by Moving-Window Two-Dimensional Correlation Spectroscopy. *J. Raman Spectrosc.* **2016**, *47*, 1375–1384.

(41) Yan, C.; Li, H.; Zhang, J.; Ozaki, Y.; Shen, D.; Yan, D.; Shi, A.-C.; Yan, S. Surface-Induced Anisotropic Chain Ordering of Polycaprolactone on Oriented Polyethylene Substrate: Epitaxy and Soft Epitaxy. *Macromolecules* **2006**, *39*, 8041–8048.

(42) Tretinnikov, O. N.; Zagorskaya, S. A. Determination of the Degree of Crystallinity of Poly(Vinyl Alcohol) by FTIR Spectroscopy. *J. Appl. Spectrosc.* **2012**, *79*, 521–526.

(43) Schenzel, K.; Fischer, S.; Brendler, E. New Method for Determining the Degree of Cellulose I Crystallinity by Means of FT Raman Spectroscopy. *Cellulose* **2005**, *12*, 223–231.

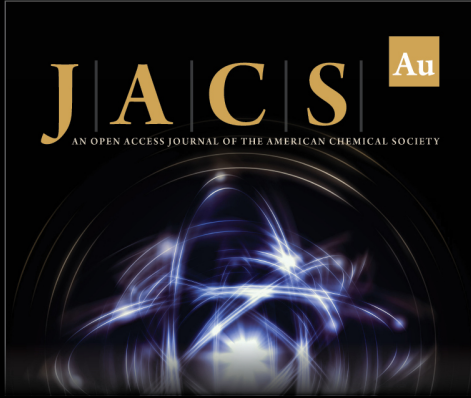
(44) Kotula, A. P.; Snyder, C. R.; Migler, K. B. Determining Conformational Order and Crystallinity in Polycaprolactone via Raman Spectroscopy. *Polymer* **2017**, *117*, 1–10.

(45) Murphy, S. H.; Leeke, G. A.; Jenkins, M. J. A Comparison of the Use of FTIR Spectroscopy with DSC in the Characterisation of Melting and Crystallisation in Polycaprolactone. *J. Therm. Anal. Calorim.* **2012**, *107*, 669–674.


(46) Flory, P. J.; Yoon, D. Y. Molecular Morphology in Semicrystalline Polymers. *Nature* **1978**, *272*, 226–229.


(47) Fritzsche, K. J.; Mao, K.; Schmidt-Rohr, K. Avoidance of Density Anomalies as a Structural Principle for Semicrystalline Polymers: The Importance of Chain Ends and Chain Tilt. *Macromolecules* **2017**, *50*, 1521–1540.


(48) Yeh, I. C.; Lenhart, J. L.; Rutledge, G. C.; Andzelm, J. W. Molecular Dynamics Simulation of the Effects of Layer Thickness and Chain Tilt on Tensile Deformation Mechanisms of Semicrystalline Polyethylene. *Macromolecules* **2017**, *50*, 1700–1712.



JACS Au
AN OPEN ACCESS JOURNAL OF THE AMERICAN CHEMICAL SOCIETY

 Editor-in-Chief
Prof. Christopher W. Jones
Georgia Institute of Technology, USA

Open for Submissions 

pubs.acs.org/jacsau  ACS Publications
Most Trusted. Most Cited. Most Read.